

Magnetization of the plasma sheet

Richard L. Kaufmann

Department of Physics, University of New Hampshire, Durham, New Hampshire, USA

W. R. Paterson and L. A. Frank

Department of Physics and Astronomy, University of Iowa, Iowa City, Iowa, USA

Received 17 July 2003; revised 18 May 2004; accepted 29 June 2004; published 30 September 2004.

[1] Long-term-averaged three-dimensional data-based models were made of the $-30 < x < -10$, $|y| < 15$, $|z| < 5 R_E$ plasma sheet region. The average magnetic moments $\langle \mu \rangle$ and Chew-Goldberger-Low (CGL) double adiabatic parameters α_{\perp} and α_{\parallel} were evaluated for ions and electrons. It was shown that restricting the observations to those taken within $0.2 R_E$ of the $B_x = 0$ point gave both a good determination of conditions at the neutral sheet and enough data points for reliable averages. Large pitch angle anisotropies would develop if the CGL parameters were constant along drift paths. In contrast, pitch angle scattering was so rapid that the observed plasma remained almost isotropic and it was the CGL parameters that varied markedly along the drift paths. Frequent ion scattering is explained by the chaotic nature of ion orbits, but electrons usually spiral around magnetic field lines even at the neutral sheet. Electron scattering by an average of 90° was needed during the 1 min it takes for a typical flux tube to undergo a net earthward displacement of $0.1 R_E$. A fast flow flux tube could move several Earth radii during this characteristic scattering time period. Rapid electron scattering also provides a mechanism to divert perpendicular current to form Birkeland current, produces diffusion, and generates a heat flux. The long-term-averaged magnetization vector \mathbf{M} was evaluated and used to calculate the magnetization or bound current density $\mathbf{j}_m = \nabla \times \mathbf{M}$. The magnetization current and an almost oppositely directed perpendicular free or guiding center drift current \mathbf{j}_f were strongest near the neutral sheet. Their sum, the total perpendicular current density \mathbf{j}_{\perp} , was an order of magnitude smaller than either \mathbf{j}_m or \mathbf{j}_f in this region. *INDEX TERMS:* 2764 Magnetospheric Physics: Plasma sheet; 2744 Magnetospheric Physics: Magnetotail; 2708 Magnetospheric Physics: Current systems (2409); 2760 Magnetospheric Physics: Plasma convection; *KEYWORDS:* electric currents, magnetotail, plasma sheet

Citation: Kaufmann, R. L., W. R. Paterson, and L. A. Frank (2004), Magnetization of the plasma sheet, *J. Geophys. Res.*, *109*, A09212, doi:10.1029/2003JA010148.

1. Introduction

1.1. Three-Dimensional Data-Based Models

[2] This paper is based on an analysis of three-dimensional (3-D) long-term-averaged data-based models of particles and fields in the plasma sheet. Magnetic fields were measured on the Geotail satellite by the magnetic field (MGF) detectors [Kokubun *et al.*, 1994], and particle measurements were made by the comprehensive plasma instrumentation (CPI) detectors [Frank *et al.*, 1994]. Plasma and field measurements were averaged within boxes spread throughout the $-30 < x < -10 R_E$, $|y| < 15 R_E$ region. Both $3 \times 3 R_E$ and $6 \times 6 R_E$ x - y boxes were used with 6 years of data. The ion count rates were low near the plasma sheet boundary layer and in the lobes, so the present analysis was limited to the central plasma sheet (CPS), or the region from the neutral sheet out to $|z| = 5 R_E$.

[3] The techniques used to create data-based models were described by Kaufmann *et al.* [2002]. Briefly, the observations first were sorted into boxes according to the GSM x and y trajectory locations and $\beta_x = P/P_{B_x}$. In this expression, P is the isotropic part of the ion plus electron pressure tensor, and $P_{B_x} = B_x^2/2\mu_0$ is the magnetic field pressure associated with only the x component of \mathbf{B} . The β_x sorting parameter was used rather than the ordinary plasma β because β_x becomes infinite at the neutral sheet, which is defined here as the sheet on which $B_x = 0$. Data points having very large β_x therefore are present during every crossing of the neutral sheet. Sorting on the basis of the ordinary β can completely miss current sheet crossings for which β never exceeds whatever value is selected to define the neutral sheet region.

[4] After sorting data into (x, y, β_x) boxes the z location of each box was calculated using the momentum equation and the assumption of long-term-averaged x force balance [Kaufmann *et al.*, 2002]. Calculating the z thicknesses of the boxes determines the shape of each field line and assures

that the x components of the electromagnetic, inertial, and pressure forces are balanced in the 3-D models. The full pressure tensor was used to calculate the pressure force. Force balance in the z direction and charge neutrality also were assured by adjusting ion and electron calibration factors. *Kaufmann et al.* [2001] described the calibration procedure, and Figure 10 of their study showed how well z forces were balanced in models based on 2 years of data. The force-balanced feature is one of the principal advantages of the plasma and field models used here. All z values in this paper refer to these calculated distances from the neutral sheet. The GSM z location of the trajectory was not used anywhere in the analysis. Finally, the data were interpolated to a fixed set of z locations to produce a uniform (x, y, z) array of averaged fluid parameters.

[5] One limitation of this study is that only long-term averages of the fluid parameters could be evaluated. The minute-to-minute variations of some parameters were larger than their long-term averages [*Angelopoulos et al.*, 1993; *Borovsky et al.*, 1997]. Another limitation arose because the techniques used to create the 3-D models treated \mathbf{B} and all plasma parameters in the same manner. The components of \mathbf{B} were simply averaged in each (x, y, β_x) box. This resulted in the consistent treatment of all particle and field averages and derivatives. We could not, however, retain the desired simplicity and consistency of the analysis and also add the requirement that $\nabla \cdot \mathbf{B} = 0$. In contrast, empirical magnetic field models use analytic expressions for \mathbf{B} or the vector potential \mathbf{A} , which contain adjustable parameters that are fit to give a good approximation to the measurements. These models are constrained to maintain $\nabla \cdot \mathbf{B} = 0$ to a high degree of accuracy [*Tsyganenko and Stern*, 1996]. We evaluated $\nabla \cdot \mathbf{B}/\nabla \times \mathbf{B}$ in each box to see how much the model $\nabla \cdot \mathbf{B}$ deviated from zero. The average magnitude of this ratio was typically ~ 0.1 or less throughout the studied region.

1.2. Fluid Parameters

[6] *Kaufmann et al.* [2001, 2002, 2003] concentrated on the average 3-D distributions of parallel and perpendicular electric current densities, particle pressure, and the anisotropies of electron and ion distribution functions. This paper investigates the contributions of ions and electrons to several parameters related to the long-term-averaged or static plasma magnetization vector

$$\mathbf{M} = \sum_{\sigma} n_{\sigma} \langle \boldsymbol{\mu}_{\sigma} \rangle, \quad (1)$$

where n_{σ} is the number density of particles of species σ . The magnitude of the magnetic moment is $\mu_{\sigma} = m_{\sigma} v_{\perp\sigma}^2 / 2B$ for a single nonrelativistic particle which is spiralling around a magnetic field line, where $v_{\perp\sigma}$ is the perpendicular velocity and m_{σ} is the mass. The average magnetic moment for a distribution of particles can be written as

$$\langle \boldsymbol{\mu}_{\sigma} \rangle = -T_{\perp\sigma} \mathbf{B} / B^2, \quad (2)$$

where the temperature T is expressed in energy units. The closely related Chew-Goldberger-Low (CGL) double adiabatic equations [*Chew et al.*, 1956] are discussed in section 3.

[7] Section 4 contains plots of M . The magnetization or bound current density

$$\mathbf{j}_m = \nabla \times \mathbf{M} \quad (3)$$

and the perpendicular part of the free or guiding center drift current density $\mathbf{j}_f = \nabla \times \mathbf{H}$ are evaluated in section 5. The term ‘‘magnetization current’’ will be used in the remainder of this paper instead of ‘‘bound current,’’ which is more commonly used in electrodynamics, because \mathbf{M} is the parameter that is determined by the observations. In contrast, the term ‘‘free current,’’ which is typically used in electrodynamics, will be used rather than ‘‘guiding center drift current’’ in this paper. The term free current was selected to avoid confusion because ions in the plasma sheet follow various chaotic orbits rather than the typical spiral orbits usually associated with guiding center studies. The major physical difference between \mathbf{j}_m and \mathbf{j}_f is that magnetization currents do not involve any net displacement of a particle after one orbital period. Magnetization currents therefore are divergence-free and cannot be diverted to form Birkeland currents. The free currents involve a net displacement of particles after one orbit, so they can transfer charge to or from the point at which perpendicular current is diverted to form Birkeland currents.

[8] In one relevant study, *Kan and Baumjohann* [1990] used Active Magnetosphere Particle Tracer Explorers/Ion Release Module data to determine the average ion magnetic moment. This paper also included a discussion of the CGL equations. Several satellite experiments have shown that the plasma is nearly isotropic at the neutral sheet [*Stiles et al.*, 1978; *Kistler et al.*, 1992; *Kaufmann et al.*, 2002]. Processes that can maintain isotropy have been studied by *Heinemann and Wolf* [2001], who compared effects of elastic scattering to effects of thermalization in the plasma sheet. This work was carried out in connection with global simulations. Here we investigate particle scattering rates from the long-term-averaged data-based modeling perspective.

[9] This paper emphasizes 3-D aspects of the central plasma sheet. Three-dimensional information reveals the changes of fluid parameters both along an average flux tube and also in the x and y directions at the neutral sheet. This latter information allows one to follow changes that would be seen by an observer moving at the average drift velocity.

2. Magnetic Moments

[10] Chaotic orbital motion results in the breakdown of the ion magnetic moment adiabatic invariant μ_i near $z = 0$ beyond about $x = -10 R_E$ [*Chen and Palmadesso*, 1986; *Büchner and Zelenyi*, 1989; *Kaufmann et al.*, 1994; *Delcourt and Martin*, 1999]. As a result, most anisotropic ion distribution functions $f_i(\mathbf{v})$ that are incident on the neutral sheet will leave having an approximately isotropic angular distribution.

[11] Typical electron orbits are not chaotic in the average field studied here. If μ_e was conserved and all electrons drifted together, then electron drift paths in the neutral sheet would be the same as the contours of constant average electron magnetic moment magnitude $\langle \mu_e \rangle$. Sections 2.1–2.3 will describe a practical method to determine $\langle \mu_{\sigma} \rangle$ at the neutral sheet from the data and will examine constant $\langle \mu_{\sigma} \rangle$ contours. A quantitative estimate of the pitch angle scattering time constant is presented in section 3.

2.1. Variations Along a Flux Tube

[12] Figure 1 shows the field lines obtained using 6 years of Geotail data. Field lines were traced starting at $z = 0$ and

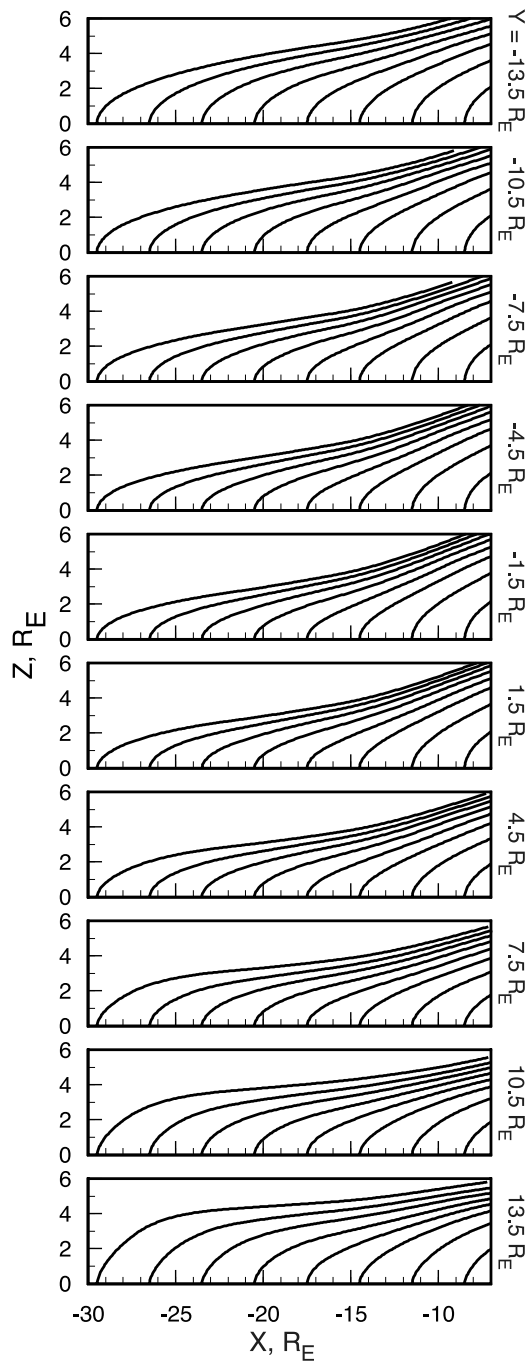


Figure 1. The x, z projections of eight magnetic field lines. The lines start at $z = 0$ and at the y locations listed at the right side of the panel. Six years of Geotail data were combined to create this model.

at the y given at the right side of each panel. A new set of field lines was traced for each model run, but the magnetic field structure was never significantly different from that shown in Figure 1 for the runs described in this paper.

[13] Figures 2a and 2b show how $\langle \mu_i \rangle$ and $\langle \mu_e \rangle$, as defined by equation (2), vary along the eight field lines in the $y = 1.5 R_E$ panel of Figure 1. Changes seen along field lines at other y locations are similar. The dramatic increases shown in Figure 2 near the most distant or neutral sheet ends of

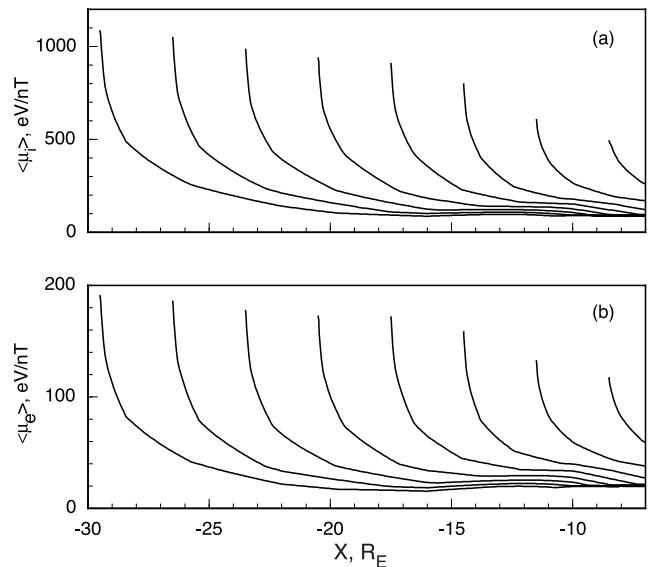


Figure 2. Average (a) ion and (b) electron magnetic moments along the eight field lines shown in the $y = 1.5 R_E$ panel of Figure 1.

each flux tube are associated with the decrease of B in this region. This strong variation of $\langle \mu_\sigma \rangle$ along \mathbf{B} does not imply that μ_σ of an individual particle is changing as it moves along a magnetic field line. Particles with large μ_σ simply mirror very close to the neutral sheet, so those with small μ_σ dominate in regions with large B . The average B at the neutral sheet is ~ 3 nT at $x = -30 R_E$, ~ 5 nT at $x = -20 R_E$, and ~ 12 nT at $x = -10 R_E$. The typical B at the most earthward end of each curve is ~ 40 nT.

[14] In order to investigate the importance of scattering, diffusion, and parallel heat flux, it is necessary to examine the x - y variations at the neutral sheet of $\langle \mu_\sigma \rangle$ and other parameters that would remain constant along drift paths if there were no scattering. The neutral sheet is the only location in a flux tube that is accessible to all particles. Figure 2 makes it clear that the data used to determine the averages must be restricted to a region very close to $z = 0$ in order to evaluate $\langle \mu_\sigma \rangle$ at the neutral sheet. For example, our model shows that $\beta = 1$ and $B = 15$ nT at approximately $|z| = 3.5 R_E$. Figures 1 and 2 show that the use of $\langle \mu_\sigma \rangle$ based on all $B < 15$ nT or $\beta > 1$ data would not give a worthwhile estimate of $\langle \mu_\sigma \rangle$ at the neutral sheet. On the other hand, if the data set is restricted too severely to a region extremely close to $z = 0$, then statistical errors become too large for us to draw useful contours of constant $\langle \mu_\sigma \rangle$ [Borovsky *et al.*, 1998].

[15] Figures 2 (see also Figures 3, 4, 6, 7, and 8) involving $\langle \mu_\sigma \rangle$ and the CGL parameters are based on geometric averages. Linear averages were evaluated for all fluid parameters and were used to calculate the z locations of each box. Geometric averages can be evaluated only for those parameters which do not change sign from point to point. One problem with using linear averages for variables which involve ratios of measured parameters is that if the denominator varies a great deal within one (x, y, β_x) box, a few points with very small denominators can dominate the averages within the box. For example, $\langle 1/B \rangle$ was signifi-

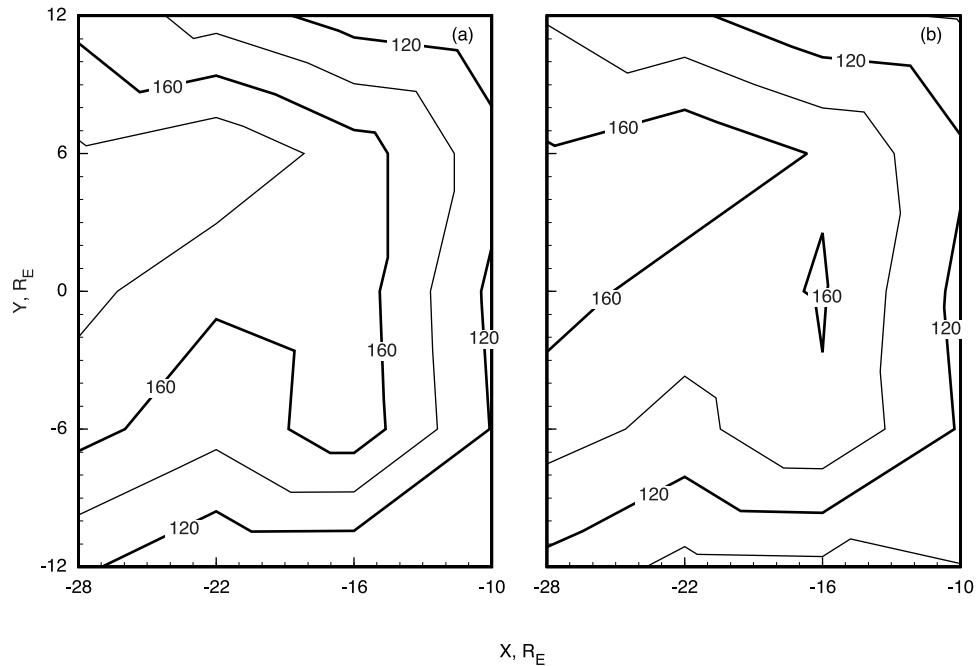


Figure 3. Average electron magnetic moments in eV/nT determined using (a) only $\beta_x > 300$ data and (b) only $\beta_x > 100$ data.

cantly different from $1/\langle B \rangle$ when linear averages were taken. In contrast, the above two ratios are the same when using geometric averages. Contours of $\langle \mu_\sigma \rangle$ based on linear averages had magnitudes $\sim 50\%$ larger than those in Figure 2. The shapes of the $\langle \mu_\sigma \rangle$ contours were similar for the two averaging methods. The differences between linear and geometric averages can be much larger for other parameters, as will be discussed in section 3. Averaging methods also become important when dealing with products or ratios of correlated parameters.

2.2. Determining $\langle \mu_e \rangle$ at the Neutral Sheet

[16] Figure 3 shows contour plots of $\langle \mu_e \rangle$ near the neutral sheet. Figure 3a used averages of all data with $\beta_x > 300$, and Figure 3b used all $\beta_x > 100$ data. The average thickness of the $\beta_x > 300$ boxes, as obtained by the analysis that determines z for each box edge, was $0.2 R_E$. The average thickness of the $\beta_x > 100$ boxes was $0.4 R_E$. Within each $6 \times 6 R_E$ x - y box, there were ~ 2000 one-minute-averaged data points per $\beta_x > 300$ box at $x = -30 R_E$ and ~ 1000 points per $\beta_x > 300$ box at $x = -10 R_E$. The number of points per box increased to >3000 and >2000 at $x = -30$ and $-10 R_E$, respectively, when $\beta_x > 100$ boxes were used.

[17] The contours in Figures 3a and 3b are similar except for an $\sim 10\%$ increase in magnitudes when the $\beta_x > 300$ averages were used. This similarity shows that averaging using only data that come from the $\beta_x > 300$ regions provides a practical way to determine $\langle \mu_e \rangle$ at the neutral sheet for flux tubes throughout the region surveyed by Geotail. There are enough $\beta_x > 300$ data points to give averages with reasonably small statistical errors. This identification of a technique to determine $\langle \mu_\sigma \rangle$ at the neutral sheet from the available data is the reason why variations of $\langle \mu_\sigma \rangle$ along magnetic field lines were examined. The remainder of the plots in this paper involving P_{\parallel} and P_{\perp} used only data from $\beta_x > 300$ regions.

2.3. Variations of $\langle \mu_i \rangle$ Along Drift Paths

[18] Figure 4 shows the plot of $\langle \mu_i \rangle$ obtained using equation (2) and only $\beta_x > 300$ data points. As for electrons, the plots generated using $\beta_x > 100$ data points were similar, with slightly smaller magnitudes.

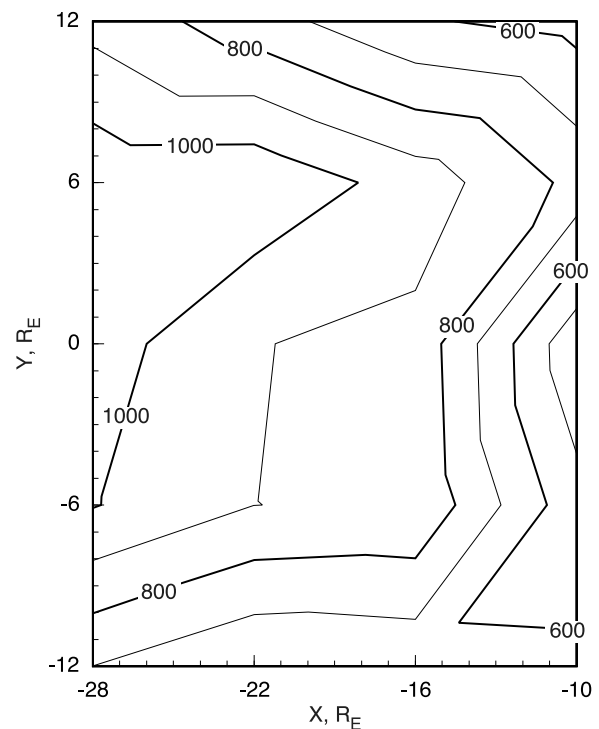


Figure 4. Average ion magnetic moments in eV/nT determined using only $\beta_x > 300$ data points.

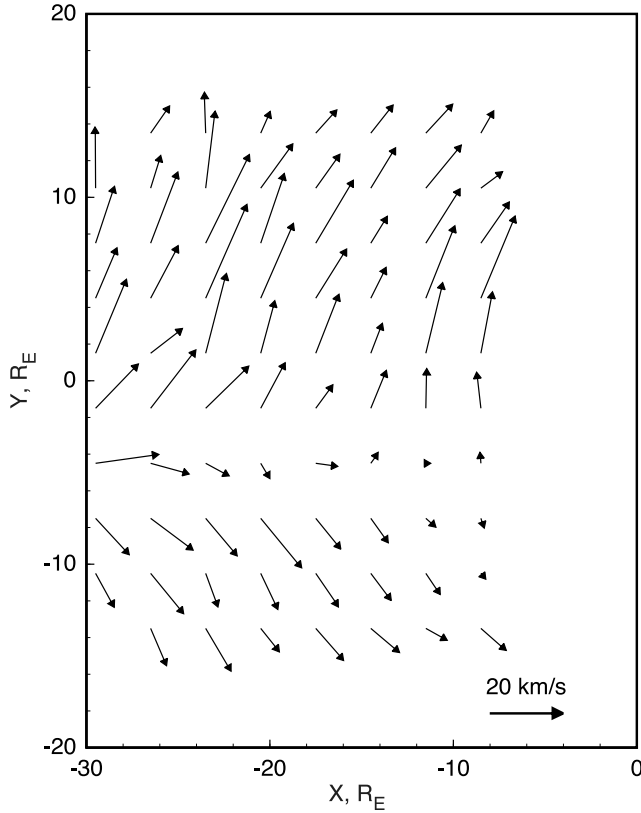


Figure 5. Average ion perpendicular flow vectors for $1.5 < |z| < 2.5 R_E$.

[19] Figure 5 shows the ion perpendicular bulk velocity $\mathbf{u}_{\perp i}$ based only on measurements made at $1.5 R_E < |z| < 2.5 R_E$ and averaged over $3 \times 3 R_E$ x - y boxes. The perpendicular bulk velocities tended to be largest at the neutral sheet and to decrease as $|z|$ increases. Averages of the x component $u_{\perp xi}$ and y component $u_{\perp yi}$ of $\mathbf{u}_{\perp i}$ were 70 and 25% larger, respectively, in the $|z| < 0.2 R_E$ box than the velocities in Figure 5. However, there were many fewer data points in the thin $|z| < 0.2 R_E$ boxes, so these averages gave a much more erratic pattern than that shown in Figure 5. Using $6 \times 6 R_E$ boxes produced a smooth flow pattern which was qualitatively similar to Figure 5 even at $|z| < 0.2 R_E$ but contained only one fourth as many independently evaluated flow vectors. At $|z| = 5 R_E$ the average $u_{\perp xi}$ was less than half that in Figure 5. The average $u_{\perp yi}$ was small and erratic at $|z| = 5 R_E$, with most measurements showing flow from dusk to dawn rather than the dawn to dusk pattern in Figure 5.

[20] Angelopoulos *et al.* [1993], Huang and Frank [1994], Paterson *et al.* [1998], and Hori *et al.* [2000] presented qualitatively similar flow patterns based on data from several satellites. These results all involved averages over much thicker z regions, e.g., using all data with $\beta > 0.5$, so they could not study the z dependence of flow velocities.

[21] One conclusion from Figures 3–5 is that the contours of constant $\langle \mu_{\sigma} \rangle$ do not resemble the observed flow patterns. This shows that $\langle \mu_e \rangle$ and $\langle \mu_i \rangle$ were not constant along drift paths. However, the variations of $\langle \mu_{\sigma} \rangle$ were relatively modest. The averages in Figures 3 and 4 remained

within $\sim 25\%$ of $\langle \mu_e \rangle = 160$ eV/nT and $\langle \mu_i \rangle = 800$ eV/nT throughout the region studied.

3. CGL Double Adiabatic Parameters

[22] The CGL double adiabatic magnetohydrodynamic (MHD) relations have been used in many geophysical studies. Recent papers have used these relations to examine low-frequency waves [Ferrière and André, 2002], interchange and bursty bulk flows [Ji and Wolf, 2003], the magnetosheath [Hau, 1996; Samsonov and Pudovkin, 2000], and collisionless shocks [Guéret *et al.*, 1998]. Some of these papers introduced more general versions of double adiabatic relations [Hau, 1996; Samsonov and Pudovkin, 2000]. Here we will only consider the original CGL parameters and examine which of the assumptions associated with their invariance fail.

[23] The CGL equations were derived by expanding $f(\mathbf{v})$ in powers of a small parameter, substituting this into the collisionless Boltzmann equation, and integrating. The expansion assumed that the plasma was quasi-uniform, with the characteristic length for spatial variations being much larger than the gyroradius and the Debye length [Chew *et al.*, 1956; Rossi and Olbert, 1970]. Similarly, the plasma was assumed to be quasi-static, with only small variations during a cyclotron period or during an electron plasma oscillation period. The derivation also assumed that $E_{\parallel} = 0$, or that conductivity was infinite along a field line, and that the pressure tensor was diagonal and gyrotopic in the magnetic field aligned frame

$$\mathbf{P}_{\sigma} = P_{\perp\sigma} \mathbf{1} + (P_{\parallel\sigma} - P_{\perp\sigma}) \hat{\mathbf{b}}\hat{\mathbf{b}}, \quad (4)$$

where $\mathbf{1}$ is the unit tensor and $\hat{\mathbf{b}}$ is a unit vector along \mathbf{B} . The infinite set of fluid equations obtained by the expansion procedure was cut off by assuming that the parallel heat flux can be neglected. If all of the above assumptions are valid, then the CGL parameters

$$\alpha_{\perp\sigma} = \frac{P_{\perp\sigma}}{n_{\sigma} B} \quad (5)$$

$$\alpha_{\parallel\sigma} = \frac{P_{\parallel\sigma} B^2}{n_{\sigma}^3} \quad (6)$$

are constant along drift paths. These parameters can be combined, giving

$$\alpha = (\alpha_{\perp}^2 \alpha_{\parallel})^{1/3} = \left[\frac{P_{\perp}^2 P_{\parallel}}{n^5} \right]^{1/3}. \quad (7)$$

There are many geophysical situations for which the assumptions needed to derive the CGL relations are not valid, so that $\alpha_{\perp\sigma}$ and $\alpha_{\parallel\sigma}$ change along drift paths. The purpose of this section is to examine the spatial variations of the long-term-averaged $\alpha_{\perp\sigma}$ and $\alpha_{\parallel\sigma}$ at the neutral sheet. A study of these variations will provide quantitative information regarding the breakdown of some assumptions.

[24] Since equation (5) is essentially the same as the magnitude of the average magnetic moment equation (2), Figures 3 and 4 also illustrate the observed variations of

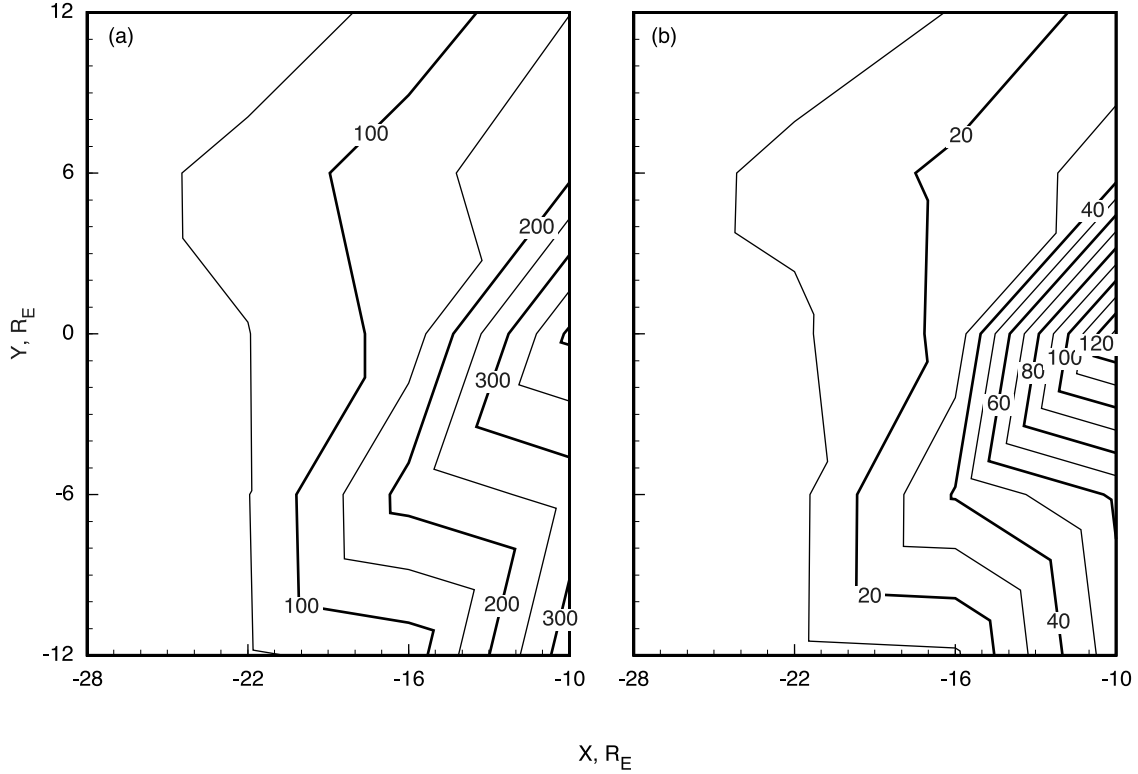


Figure 6. CGL α_{\parallel} parameter in $\text{nPa nT}^2 \text{cm}^9$ determined using $\beta_x > 300$ data points for (a) ions and (b) electrons.

$\alpha_{\perp\sigma}$ within the neutral sheet. *Kan and Baumjohann* [1990] showed that for the simple case of particles confined between moving mirror points within a flux tube or magnetic bottle, conservation of $\alpha_{\parallel\sigma}$ is approximately equivalent to conservation of the second adiabatic invariant. Figure 6a shows $\alpha_{\parallel i}$, and Figure 6b shows $\alpha_{\parallel e}$ in the $\beta_x > 300$ boxes. The structure was similar except that the magnitudes were $\sim 20\%$ larger in plots using $\beta_x > 100$ data. The n^3 and B^2 factors in $\alpha_{\parallel\sigma}$ created the largest differences we found between the use of linear and geometric averages to evaluate any parameter. At the neutral sheet the quantity $\langle B^2/n^3 \rangle$ differed by up to a factor of 1000 from $1/\langle n^3/B^2 \rangle$ when using linear averages. These two quantities are equal for the geometric averages used in Figure 6.

[25] Figures 3–6 show that the contours of constant $\alpha_{\perp\sigma}$ and $\alpha_{\parallel\sigma}$ bear little resemblance to drift paths. Figure 6 shows that $\alpha_{\parallel\sigma}$ increases by at least an order of magnitude when moving from $x = -30$ to $-10 R_E$, while Figures 3 and 4 show that $\alpha_{\perp\sigma}$ increases by less than a factor of 2 when going from $x = -10$ to $-30 R_E$. Since $\alpha_{\perp\sigma}$ is the averaged first adiabatic invariant and $\alpha_{\parallel\sigma}$ is more closely associated with the second invariant, we conclude that violations of the second invariant are much larger than violations of the first invariant.

[26] One way to appreciate the magnitude of the differences between the observations and the results that would be obtained if $\alpha_{\parallel\sigma}$ and $\alpha_{\perp\sigma}$ were conserved is to note that

$$\frac{P_{\parallel\sigma}}{P_{\perp\sigma}} = \frac{\alpha_{\parallel\sigma} n_{\sigma}^2}{\alpha_{\perp\sigma} B^3} \quad (8)$$

so that the average $P_{\parallel\sigma}/P_{\perp\sigma}$ ratio would vary as n_{σ}^2/B^3 if $\alpha_{\parallel\sigma}$ and $\alpha_{\perp\sigma}$ were constant. Figure 7 is a plot of n_i^2/B^3 . The

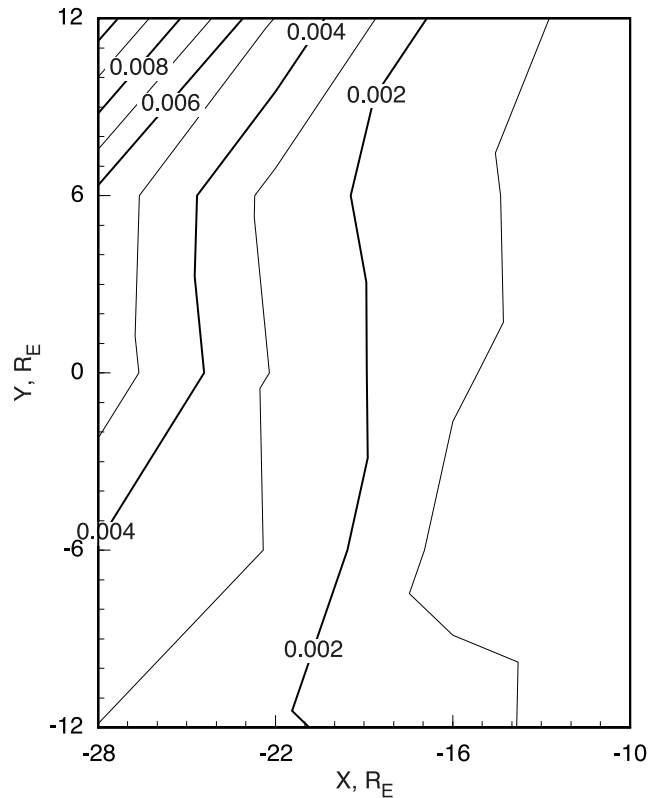


Figure 7. Ratio n_i^2/B^3 in $\text{cm}^{-6} \text{nT}^{-3}$ determined using $\beta_x > 300$ data points.

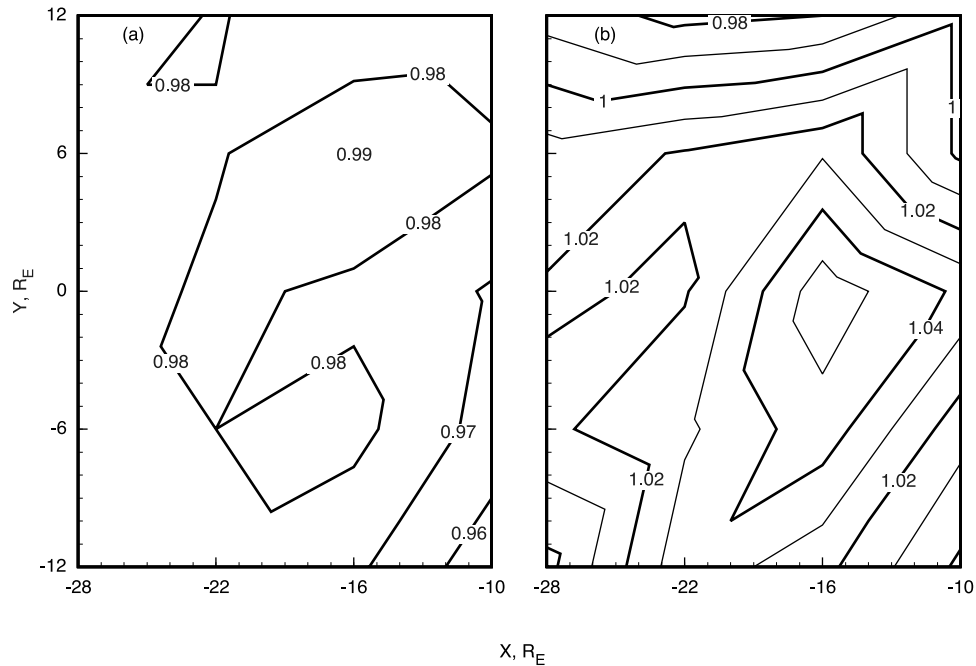


Figure 8. Average pressure anisotropy P_{\parallel}/P_{\perp} of (a) ions and (b) electrons determined using $\beta_x > 300$ data points.

model n_i and n_e are almost equal. It is seen that $P_{\parallel\sigma}/P_{\perp\sigma}$ would be ~ 10 times larger in the most distant boxes than it is in the boxes nearest the Earth for both ions and electrons if $\alpha_{\parallel\sigma}$ and $\alpha_{\perp\sigma}$ were constant. Figures 8a and 8b show the measured $P_{\parallel\sigma}/P_{\perp\sigma}$ ratio for ions and electrons, respectively, using data from the $\beta_x > 300$ boxes. Instead of changing by a factor of 10, it is seen that the long-term-averaged $P_{\parallel\sigma}/P_{\perp\sigma}$ ratios are usually within 2% of 1.00 throughout the neutral sheet. The pressure anisotropy is significantly larger during short time intervals. The standard deviations of the 1-min-averaged $P_{\parallel\sigma}/P_{\perp\sigma}$ ratios were $\sim 10\%$ near the neutral sheet. The anisotropy also was examined using $3 \times 3 R_E$ boxes to see if the long-term averages showed any effects of butterfly distributions, which begin to appear near the perigee of Geotail [Fritz *et al.*, 2003]. Statistics became poorer and the standard deviation was larger when using the smaller $3 \times 3 R_E$ boxes. We could not identify significant effects of butterfly distributions in the averages by examining only the $P_{\parallel\sigma}/P_{\perp\sigma}$ ratio. It is likely that such effects could be found at these altitudes if distribution functions were examined, but the data set used here includes only the fluid parameters.

[27] The pressure becomes more anisotropic as one moves away from the neutral sheet along plasma sheet field lines. This feature was analyzed by Kaufmann *et al.* [2002]. Both ions and electrons had a maximum average $P_{\parallel\sigma}/P_{\perp\sigma}$ ratio of ~ 1.1 at distances on the order of $1 R_E$ from the neutral sheet. The fact that this feature was seen throughout the plasma sheet indicated that it was not produced by adiabatic behavior associated with the drift of flux tubes. The buildup of an electron anisotropy along a flux tube was attributed to the weak parallel electric field needed to maintain charge neutrality in a region containing guiding center electrons and nonguiding center ions [Kaufmann and Lu, 1993]. The ion anisotropy was attributed to effects of chaotic orbital motion.

[28] The above observations provide some information about which of the CGL assumptions are most severely violated. The 1-min time resolution was far too slow to study either the temporal or spatial scales over which conditions are assumed to be quasi-static or quasi-uniform. All elements of the pressure tensors were measured, and the off-diagonal elements were consistently found to be very small. This supports the gyrotropic assumption. As noted above, our earlier studies concluded that an E_{\parallel} exists near the neutral sheet. This field is too weak to significantly modify the ion distribution function but can produce a 10% anisotropy of the less energetic electrons over a z distance of $1 R_E$.

[29] The observation of almost perfect isotropy at $z = 0$ strongly suggests that wave-particle scattering, or the violation of the assumption that the plasma is collisionless, is the primary cause of CGL parameter variations. The presence of scattering will result in diffusion and a parallel heat flux, which are considered to be secondary effects. For example, it would be hard to imagine any heat source or sink along a flux tube, such as at the ionospheric end, which would inherently supply or remove just enough heat so the equatorial pitch angle distribution happens to remain within 2% of complete isotropy. In contrast, strong pitch angle scattering within the plasma sheet is a physical process that would naturally remove almost all anisotropies that develop during convection.

[30] The required scattering rate can be estimated by noting that a factor of 2 change in $P_{\parallel\sigma}/P_{\perp\sigma}$ would be expected (Figure 7) as flux tubes move a distance of $5 R_E$ in the x direction. The observation that the average measured electron anisotropy rarely changes by $>2\%$ over $5 R_E$ shows that one 90° scattering event takes place as the long-term-averaged location of an electron moves earthward by $5 \times 0.02 = 0.1 R_E$. This 90° of scattering could involve the net

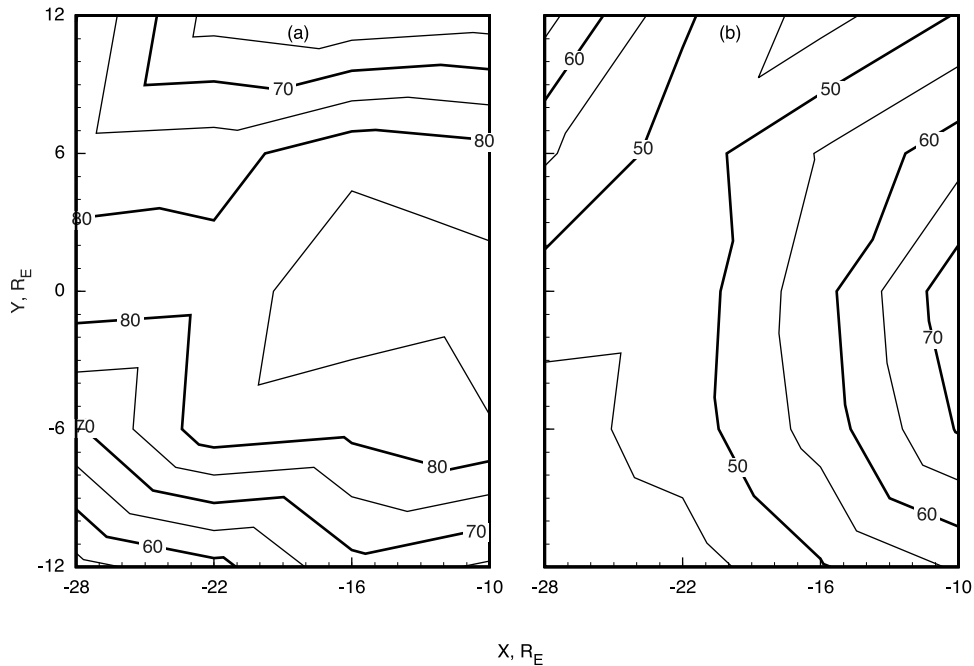


Figure 9. Magnitude of the average electron magnetization vector in $\text{eV cm}^{-3} \text{ nT}^{-1}$ at (a) $|z| < 0.2 R_E$ and (b) $0.2 < |z| < 0.7 R_E$.

effect of many small angle scattering events. Since the long-term-averaged earthward drift speed is on the order of 10 km/s, a net 90° of electron scattering is needed about every minute. Typical electron bounce times are on the order of 10 s. The chaotic ions, which become nearly isotropic during each neutral sheet interaction, have bounce times on the order of 10 min.

[31] *Angelopoulos et al.* [1993] and *Borovsky et al.* [1997] showed that fluctuations are so large that the average drift speed $\langle |v_\sigma| \rangle$ is several times larger than the magnitude of the average bulk velocity $u_\sigma = |\langle v_\sigma \rangle|$. These fluctuations will smooth the observed average variations of $\alpha_{\parallel\sigma}$ and $\alpha_{\perp\sigma}$. A typical flux tube will move back and forth by a distance on the order of $1 R_E$ during the minute required for the long-term-averaged location to move $0.1 R_E$ earthward. The CGL parameters therefore would be conserved while an average flux tube moves back and forth by $1 R_E$, or while a flux tube moves several Earth radii during a fast flow event.

4. Magnetization Vector

4.1. Electrons

[32] Figures 9a and 9b show the magnitude of the electron long-term-averaged magnetization vector $M_e = n_e \langle \mu_e \rangle$ in the $|z| < 0.2$ and $0.2 < |z| < 0.7 R_E$ boxes, respectively. Linear averages are needed in section 5, so they were used here too. The direction of \mathbf{M}_e is antiparallel to \mathbf{B} . Since electrons follow spiral orbits, μ_e and M_e have their usual meanings. Figure 9 shows that M_e varies more rapidly in the z direction than in the x and y directions, as might be expected from Figure 2.

4.2. Ions

[33] It is easy to put the measured ion parameters into equations (1) and (2) to obtain values for \mathbf{M}_i and the total plasma magnetization \mathbf{M} . The resulting constant M contours

have features similar to those seen in Figure 9, with magnitudes ~ 6 times larger. However, since ions do not spiral around field lines at the neutral sheet, the interpretation of \mathbf{M}_i is more difficult.

[34] We carried out a lengthy study of this topic in connection with a project to develop theoretical plasma sheet models using consistent orbit tracing techniques [Kaufmann et al., 1997a, 1997b]. Currents carried by various groups of energetic ions were examined [Kaufmann et al., 1997b] by accurately tracing the chaotic orbits. These results were compared with predictions based on the adiabatic guiding center approximations [Parker, 1957; Northrop, 1963], which will be examined in section 5. It was found that ions following some of these complex trajectories carry very large magnetization currents even though they do not spiral around field lines.

[35] One class of particles remained trapped, meandering back and forth across the neutral sheet. Both spiral orbits and meandering orbits have adiabatically invariant action integrals. The associated spiral orbit angle variable is $s_\perp = \rho\theta$, where $\rho = v_\perp/\Omega$ is the gyroradius, $\Omega = qB/m$ is the gyrofrequency, and θ is the azimuthal angle about \mathbf{B} . The resulting action variable

$$\oint v_\perp ds_\perp \quad (9)$$

is $4\pi\mu/q$. The meandering orbit angle variable is z , and the action variable is

$$I_z = \oint v_z dz \quad (10)$$

for nonrelativistic particles.

[36] The y - z projection of a nonguiding center trapped particle trajectory has the shape of a figure eight centered at

$z = 0$ that drifts slowly in the y direction. Figure 5 of *Larson and Kaufmann* [1996] shows a sample trapped orbit. Such orbits create strong magnetization currents \mathbf{j}_m from dusk to dawn near $z = 0$ and slightly larger \mathbf{j}_m from dawn to dusk at $z_0 < |z| < 2 z_0$, where

$$z_0 = mv / [qB_{xy}(z_0)] \quad (11)$$

is the point at which the B_{xy} magnetic field becomes strong enough to turn a particle of mass m , velocity v , and charge q back toward the neutral sheet and $B_{xy}^2 = B_x^2 + B_y^2$. In the magnetic field model shown in Figure 1, z_0 is $\sim 0.7 R_E$ for a typical observed ion and shows little dependence on x or y . A particle on a figure eight orbit that did not drift would return to its starting point after one oscillation period, so it would carry no free current. The strong downward \mathbf{j}_m at $|z| < z_0$ and the strong duskward \mathbf{j}_m at $z_0 < |z| < 2 z_0$ would cancel if integrated from $z = 0$ to $|z| > 2 z_0$.

[37] Whereas trapped particles remain near the neutral sheet for an extended period of time, *Speiser* [1965] investigated a class of nonguiding center orbits that mirror at low altitudes and spend only brief intervals near the neutral sheet. Speiser particles spiral around field lines for most of such an orbit and cross an orbital separatrix near $|z| = 2 z_0$. These particles then meander back and forth across the neutral sheet for a short period as they drift along a path with a semicircular projection in the x - y plane. After this, they leave the neutral sheet region to resume spiral motion. Although μ is nearly constant during the spiral portions of these orbits and I_z is nearly constant during the meandering portion, in general, neither is conserved near the separatrix. The magnetic moment often is substantially different before and after the neutral sheet interaction. Most of the net drift of a Speiser particle takes place while it is at $|z| < 2 z_0$. This free current \mathbf{j}_f is from dawn to dusk in the neutral sheet. A weak dusk to dawn current is present beyond $|z| = 2 z_0$ [*Kaufmann et al.*, 1997b].

[38] The orbits of nonguiding center particles with mirror points intermediate between the trapped and Speiser extremes have been referred to as cucumber orbits [*Büchner and Zelenyi*, 1989]. Depending on their distribution of mirror points, a group of such particles can carry cross-tail current in either direction at the neutral sheet. The cross-tail current is from dusk to dawn at $|z|$ somewhat smaller than the average location of the mirror point of a group of cucumber particles and from dawn to dusk at larger $|z|$. Figures 2 and 3 of *Larson and Kaufmann* [1996] show typical Speiser orbits, with mirror points far away from the neutral sheet, and cucumber orbits, with mirror points closer to the neutral sheet but beyond $|z| = 2 z_0$.

[39] The chaotic nature of plasma sheet ions often causes them to move from one type of orbit to another during a neutral sheet interaction. The resulting substantial change in mirror points from orbit to orbit shows that the second adiabatic invariant changes markedly. The angle variable is s , the arc length along a field line, for the second invariant action variable

$$J = \oint mv_{\parallel} ds. \quad (12)$$

[40] When a group of particles was specifically selected so that it was dominated by ions on trapped orbits or by ions

on Speiser orbits [*Kaufmann et al.*, 1997b], it was found that these groups carried currents that differed substantially from the currents predicted by the adiabatic guiding center drift equations. These select groups had highly anisotropic distribution functions. When various groups of particles following trapped, cucumber, and Speiser orbits were mixed together to produce a nearly isotropic self-consistent plasma sheet, then the full plasma was consistently found to carry currents that were very close to those predicted by the adiabatic guiding center equations. *Usadi et al.* [1996] reached a similar conclusion by comparing the adiabatic drift equations to the actual drifts of groups of nonguiding center particles. These studies therefore show that because the overall plasma is observed to be nearly isotropic, the use of equations (1) and (2) provides a reasonable estimate of the total plasma magnetization vector. In section 5 we therefore will use equations (1), (2), and (3) to estimate \mathbf{j}_m .

5. Calculated Magnetization and Free Current Densities

[41] The total average plasma sheet current density is coupled, through Ampere's law, to the average observed magnetic field $\mathbf{j} = (1/\mu_0)\nabla \times \mathbf{B}$. For some applications it is necessary to separate the total perpendicular current into perpendicular magnetization $\mathbf{j}_{m\sigma}$ and free $\mathbf{j}_{f\sigma}$ components and to separate the currents carried by ions and electrons. For example, *Kaufmann et al.* [2003] used the 3-D data-based models to examine the buildup of parallel current j_{\parallel} within the CPS. Since $\mathbf{j}_{m\sigma}$ is divergence-free, it is only the perpendicular $\mathbf{j}_{f\sigma}$ portion of the total current that can be diverted to create a steady j_{\parallel} . Detectors in the topside ionosphere have shown that it is electrons which carry the bulk of the observed j_{\parallel} even within upgoing ion beams [*Kaufmann and Kintner*, 1984], so it is \mathbf{j}_{fe} that is of interest to studies of the source of Birkeland current in the CPS. Another reason for separating $\mathbf{j}_{f\sigma}$ and $\mathbf{j}_{m\sigma}$ is because they contribute differently to kinetic and fluid plasma instabilities [*Ichimaru*, 1973]. It is only the drift associated with $\mathbf{j}_{f\sigma}$ that is involved in the kinetic resonant particle instabilities with perpendicularly propagating plasma waves. The total perpendicular current is involved in MHD and certain other kinetic instabilities.

5.1. Adiabatic Drift Equations

[42] The adiabatic guiding center expressions for the perpendicular magnetization and free current densities are [*Parker*, 1957; *Northrop*, 1963]

$$\mathbf{j}_{m\sigma} = \frac{\mathbf{B}}{B^2} \times \left[\nabla P_{\perp\sigma} - \frac{P_{\perp\sigma}}{B} \nabla B - \frac{P_{\parallel\sigma}}{B^2} (\mathbf{B} \cdot \nabla) \mathbf{B} \right] \quad (13)$$

$$\mathbf{j}_{f\sigma} = \frac{\mathbf{B}}{B^2} \times \left[\frac{P_{\perp\sigma}}{B} \nabla B + \frac{P_{\parallel\sigma}}{B^2} (\mathbf{B} \cdot \nabla) \mathbf{B} + n_{\sigma} m_{\sigma} (\mathbf{u} \cdot \nabla) \mathbf{u} - n_{\sigma} q_{\sigma} \mathbf{E} \right] + \mathbf{j}_{c\sigma}, \quad (14)$$

and the total perpendicular current density is

$$\mathbf{j}_{\perp} = \sum_{\sigma} (\mathbf{j}_{m\sigma} + \mathbf{j}_{f\sigma}). \quad (15)$$

The magnetization current terms are the pressure or density plus temperature gradient current, the part of the ∇B current associated with the area of a gyroorbit and the period of gyration, and the part of the field line curvature current associated with orbit crowding. These terms involve only the circular component of the motion of a spiralling particle, not any net displacement of the particle's guiding center.

[43] The free current terms are the part of the ∇B drift associated with the net displacement produced by the spatially varying gyroradius of meandering particles, the centrifugal force portion of the curvature drift, polarization drift associated with spatial variations of the perpendicular bulk speed, the $\mathbf{E} \times \mathbf{B}$ drift, and diffusion associated with collisions or other scattering processes. These terms all result in a net displacement of a particle after one gyroperiod so they can continuously supply particles to a flux tube that carries a steady Birkeland current. Gravitational drift has not been included in equation (14) because its magnitude is very small in the plasma sheet. The net cross-tail displacement of chaotic particles after one full figure eight-shaped orbit, the meandering portion of Speiser orbits, and the net displacement after a full cucumber orbit all contribute to the free current.

[44] Several terms cancel when evaluating \mathbf{j}_\perp using equation (15). The ∇B terms in equations (13) and (14) cancel when $\mathbf{j}_{m\sigma}$ and $\mathbf{j}_{f\sigma}$ are added. The $\mathbf{E} \times \mathbf{B}$ terms cancel in the sum over species if the plasma is neutral. One feature that may seem confusing is that the expression typically used to evaluate j_\parallel by calculating $\nabla \times \mathbf{j}_\perp$ for an isotropic slow flow plasma involves using $\nabla \times \mathbf{j}_\perp = \nabla \cdot (\mathbf{B} \times \nabla P/B^2)$ [Vasyliunas, 1970; Wolf, 1983]. Since ∇P appears only in \mathbf{j}_m , which is divergence-free, it might seem as if this term should not appear in a calculation of j_\parallel . However, it is because $\nabla \cdot \mathbf{j}_m = 0$ that the divergence of the first term in equation (13) is equal to the divergence of the other two terms in equation (13) and therefore is the same as the divergence of the first two terms in equation (14) in an isotropic plasma. Since all other terms in equation (14) are either zero or neglected when flow is slow and the species are combined in equation (15), $\nabla \cdot \mathbf{j}_f$ is correctly given by the usual expression which contains only the ∇P term.

5.2. Current Density Evaluation Methods

[45] The technique that has almost always been used to determine \mathbf{j}_\perp in either the ionosphere [Zmuda and Armstrong, 1974; Iijima and Potemra, 1978; Weimer, 2001] or the magnetotail [Tsyganenko et al., 1993; Israelevich et al., 2001] is to use Ampere's law and measurements of \mathbf{B} . Section 4 concluded that \mathbf{M}_σ can be adequately approximated using equations (1) and (2). It therefore is possible to apply this same technique, using equation (3), to determine $\mathbf{j}_{m\sigma}$ for each species. Since the perpendicular free current density is given by $\mathbf{j}_f = \mathbf{j}_\perp - \mathbf{j}_m$, the availability of \mathbf{j}_\perp only for the sum of all species means that \mathbf{j}_f can be evaluated only for the sum of all species.

5.3. Current Density Results

[46] Figure 10 shows \mathbf{j}_\perp for the three z boxes closest to the neutral sheet and for one box at larger z . These results are based on evaluating $\nabla \times \mathbf{B}$ using all data from 6 years of measurements. The first three z boxes are from runs that kept Northern and Southern Hemisphere data separate so

that derivatives could be evaluated at the neutral sheet. The resulting values of \mathbf{j}_\perp were similar in boxes above and below the neutral sheet, so pairs of results at (x, y, z) and at $(x, y, -z)$ were averaged for the plot. Figure 10d was made by first folding Northern and Southern Hemisphere data together and then taking the derivatives. All these methods were the same as those used previously [Kaufmann et al., 2001]. The calculations of electric currents were based on linear averages. It is not possible to geometrically average the components of \mathbf{B} because the sign of each component is positive for some data points and negative for others.

[47] Figure 11 shows \mathbf{j}_m obtained using equation (3), again on the basis of linear averages. Since \mathbf{M} also could be evaluated using geometric averages, \mathbf{j}_m was calculated using both methods. The values of \mathbf{j}_m determined using linear averages were $\sim 20\%$ larger than the values of \mathbf{j}_m determined from geometric averages. The principal conclusions of this part of the analysis therefore did not depend strongly upon the averaging method used.

[48] The magnetization current is seen to be from dusk to dawn at $z < 0.7 R_E$. The very strong z dependence is partly caused by the localization of \mathbf{M} and partly because the direction of \mathbf{B} and therefore of \mathbf{M} changes rapidly near the neutral sheet. The sign of the cross-tail current fluctuates from box to box in Figure 11c but is primarily from dawn to dusk. The current is consistently from dawn to dusk at all larger z , as shown in Figure 11d. Since z_0 is $\sim 0.7 R_E$, these directions and locations are all consistent with the properties expected for chaotic particle magnetization currents, as discussed in section 4. The most important aspect of Figure 11 is that the scale differs from that in Figure 10 by a factor of 10. The magnetization current at $z < 0.2 R_E$ is more than an order of magnitude larger than the total current \mathbf{j}_\perp and in the opposite direction.

[49] Equation (3) gave $\mathbf{j}_{m\sigma}$ separately for ions and electrons. The electron magnetization current plot was similar to Figure 11 except the magnitudes were about one fifth the values for ions. This is approximately the same as the ratio of T_e/T_i in our data set, as has previously been reported using other data sets [Baumjohann et al., 1989]. These results also are just what would be expected in a nearly isotropic plasma. It is the curvature of field lines that produces most of the $\mathbf{j}_{m\sigma}$ for both electrons and the chaotic ions. For electrons the curvature term was an order of magnitude larger than the ∇B and pressure terms in equation (13).

[50] Figure 12 shows \mathbf{j}_f , or the perpendicular part of $\nabla \times \mathbf{H}$, which is simply $\mathbf{j}_\perp - \mathbf{j}_m$. Figure 12 has the same scale as Figure 11. The direction of \mathbf{j}_f is consistently from dawn to dusk only at $|z| < 0.7 R_E$. The direction of the calculated \mathbf{j}_f fluctuated in the outer z boxes. Both \mathbf{j}_\perp and \mathbf{j}_m were consistently from dawn to dusk and had similar magnitudes in the outer z boxes. Their difference, or the calculated \mathbf{j}_f , is not sufficiently accurate here to even give a reliable direction. The data-based calculations of \mathbf{j}_f are therefore useful only in the $|z| < 0.7 R_E$ boxes.

6. Discussion and Summary

[51] This paper investigated the magnetization vector \mathbf{M} and several associated parameters throughout the $-30 < x < -10 R_E$, $|y| < 15 R_E$ region of the plasma sheet. Approx-

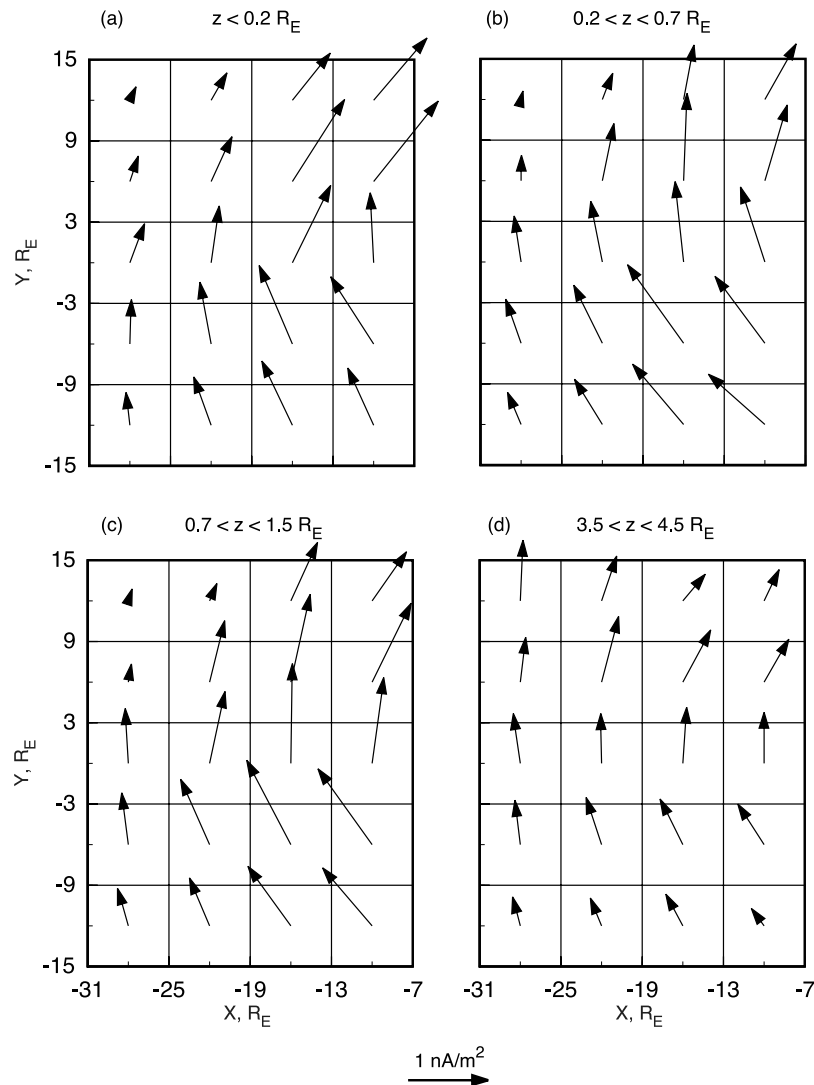


Figure 10. Total perpendicular current density \mathbf{j}_\perp in the (a) $|z| < 0.2 R_E$, (b) $0.2 < |z| < 0.7 R_E$, (c) $0.7 < |z| < 1.5 R_E$, and (d) $3.5 < |z| < 4.5 R_E$ boxes.

imately 100,000 one-minute-averaged plasma sheet data points were available per year. All data from 6 years of CPI particle and MGF measurements taken on the Geotail satellite were combined for the analysis. As a result, only long-term-averaged conditions were studied.

6.1. Average Magnetic Moments and CGL Parameters

[52] The Chew-Goldberger-Low (CGL) double adiabatic parameters $\alpha_{\perp\sigma}$ and $\alpha_{\parallel\sigma}$ [Chew *et al.*, 1956] were evaluated as a part of the data-based modeling procedure. The parameter $\alpha_{\perp\sigma}$ is essentially the same as the average magnetic moment $\langle\mu_{\sigma}\rangle$. Since $\langle\mu_{\sigma}\rangle$ varies rapidly along magnetic field lines near the equator, it was necessary to investigate this spatial dependence so a procedure could be developed to determine $\langle\mu_{\sigma}\rangle$ at the neutral sheet. We concluded that averaging all data with $\beta_x > 300$ provided both a good estimate of $\langle\mu_{\sigma}\rangle$ at $|z| < 0.2 R_E$ and enough data to give consistent results (Figures 3 and 4). It was found that $\alpha_{\perp\sigma}$ or $\langle\mu_{\sigma}\rangle$ at the neutral sheet tended to decrease as one moved earthward and toward the flanks but varied by only 25% from the value averaged throughout the region studied.

[53] Contours of constant $\alpha_{\parallel\sigma}$ changed much more dramatically in the region studied. This parameter, which is related to the second adiabatic invariant, increased by an order of magnitude when moving from the most tailward to the most earthward boxes (Figure 6). It also was shown (Figure 7) that the P_{\parallel}/P_{\perp} ratio at the neutral sheet would be expected to change by approximately a factor of 10 as particles drift through the region studied if the CGL parameters remained constant. In contrast, this ratio varied by only $\sim 2\%$ from 1.00, or perfect isotropy. Since ions follow chaotic orbits, the fact that they were scattered and became isotropic during each interaction with the neutral sheet was not surprising. However, electrons follow spiral guiding center orbits, and they remained almost equally isotropic at the neutral sheet. It was estimated that electrons were scattered by 90° in ~ 1 min, or the time required for an average flux tube to undergo a net earthward displacement of $0.1 R_E$ in the plasma sheet.

[54] The presence of strong electron and ion scattering has several important consequences. Such scattering results in diffusion and an associated parallel heat flux. Strong

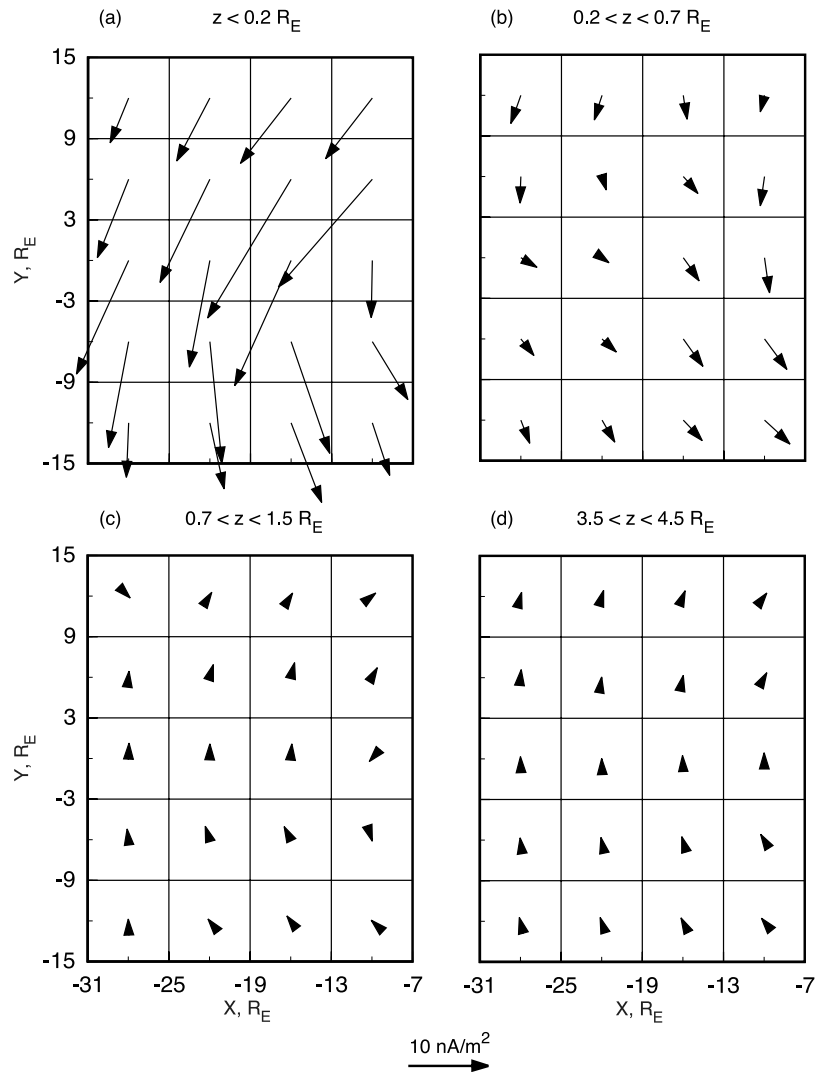


Figure 11. Magnetization current density \mathbf{j}_m in the (a) $|z| < 0.2 R_E$, (b) $0.2 < |z| < 0.7 R_E$, (c) $0.7 < |z| < 1.5 R_E$, and (d) $3.5 < |z| < 4.5 R_E$ boxes.

scattering also suggests that a collision term $(\delta f/\delta t)_c$ may be needed in the Boltzmann equation for any study of transport in the plasma sheet. In addition, the presence of electron scattering helps explain how region 1 Birkeland currents build up within the plasma sheet [Kaufmann *et al.*, 2003].

6.2. Magnetization Vector and Perpendicular Current Densities

[55] The separation of total perpendicular current density \mathbf{j}_\perp into electron and ion magnetization $\mathbf{j}_{m\sigma}$ and perpendicular free $\mathbf{j}_{f\sigma}$ current densities was examined. One reason for an interest in this separation is that $\mathbf{j}_{m\sigma}$ is divergence-free so that only the perpendicular $\mathbf{j}_{f\sigma}$ can be diverted to create parallel currents. The electron current \mathbf{j}_{fe} is of particular interest since a continuous source of electrons is needed to sustain the observed long-term-averaged Birkeland current system. Another reason it is worthwhile to separate $\mathbf{j}_{m\sigma}$ from $\mathbf{j}_{f\sigma}$ is to permit a study of instabilities. Drift waves and MHD instabilities depend upon the total current \mathbf{j}_\perp . Some kinetic instabilities involve resonances with groups of particles that are steadily drifting at the perpendicular wave propagation

velocity. Only the $\mathbf{j}_{f\sigma}$ component of \mathbf{j}_\perp can sustain this type of resonant interaction.

[56] The magnitude of the electron magnetization vector, as determined using equations (1) and (2), was plotted in Figure 9. On the basis of previous orbit tracing studies [Usadi *et al.*, 1996; Kaufmann *et al.*, 1997b] it was concluded that equations (1) and (2) can be used to estimate \mathbf{M} even for chaotic ions as long as the distribution function remains nearly isotropic, as is observed in the long-term averages (Figure 8). The average magnetization \mathbf{M} was found to be strongly concentrated near the neutral sheet.

[57] The magnetization current $\mathbf{j}_m = \nabla \times \mathbf{M}$ was calculated and compared with the total perpendicular current \mathbf{j}_\perp , determined from $\nabla \times \mathbf{B}$. It was found that \mathbf{j}_m was an order of magnitude larger than \mathbf{j}_\perp in the z box closest to the neutral sheet but that \mathbf{j}_m dropped off so rapidly that $\mathbf{j}_\perp \approx \mathbf{j}_m$ in the outer boxes studied. Separate ion and electron magnetization currents were calculated, and it was found that \mathbf{j}_{mi} was ~ 5 times as large as \mathbf{j}_{me} . The ordinary adiabatic drift equations were examined to see how much each term contributes to \mathbf{j}_{me} . It was found that the ∇B term was

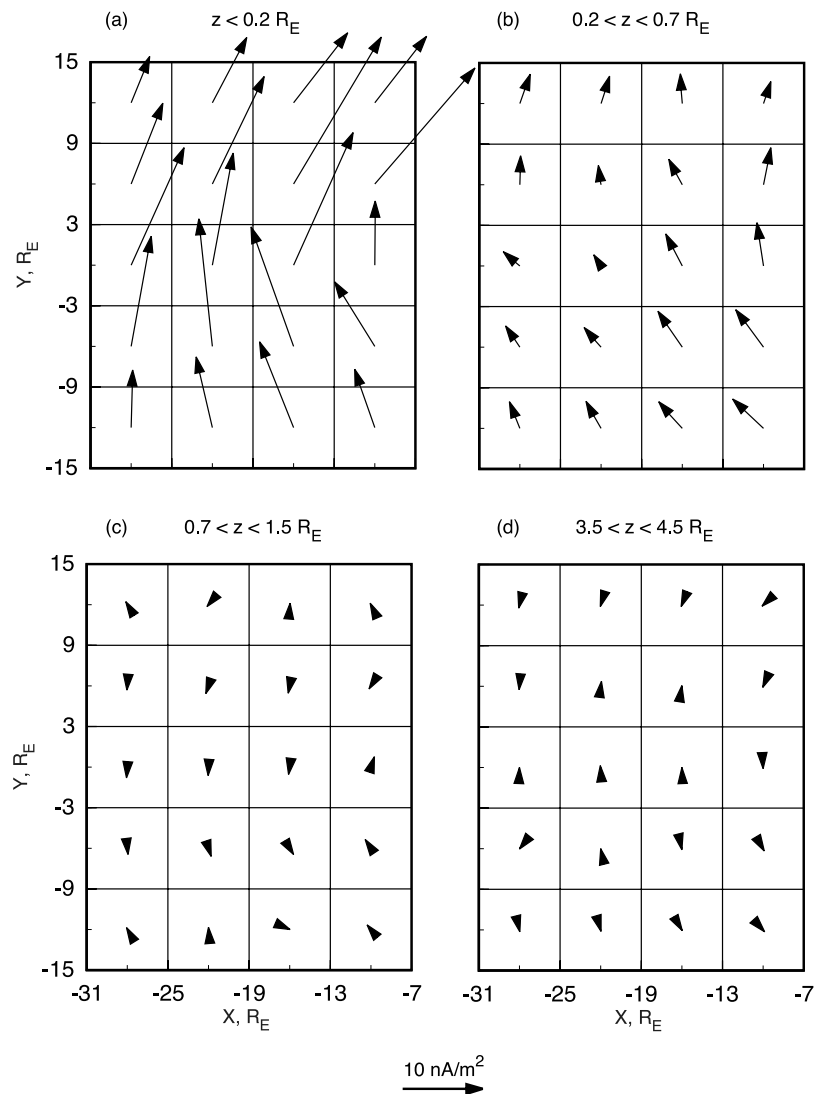


Figure 12. Perpendicular free current density \mathbf{j}_f in the (a) $|z| < 0.2 R_E$, (b) $0.2 < |z| < 0.7 R_E$, (c) $0.7 < |z| < 1.5 R_E$, and (d) $3.5 < |z| < 4.5 R_E$ boxes.

smallest, the pressure term was next largest, and the field line curvature term dominated by approximately a factor of 10.

[58] Finally, the free current \mathbf{j}_f , or the perpendicular part of $\nabla \times \mathbf{H}$, was estimated from the observations by evaluating the difference between the two currents that could be determined directly, $\mathbf{j}_f = \mathbf{j}_\perp - \mathbf{j}_m$. This procedure produced reliable results only near the neutral sheet. Since \mathbf{j}_m was an order of magnitude larger than \mathbf{j}_\perp at the neutral sheet, it is clear that \mathbf{j}_f and \mathbf{j}_m must have nearly equal magnitudes and must point in nearly opposite directions in this region.

[59] Since \mathbf{j}_e was found to be so large and highly concentrated near the neutral sheet, it might at first be expected that the neutral sheet is the principal source of Birkeland current. Our recent paper [Kaufmann *et al.*, 2003] used the data-based models to study the origin of parallel currents in the plasma sheet. When data from all IMF orientations were combined, we concluded that j_{\parallel}/B , the long-term-averaged parallel current within a unit flux tube, built up throughout much of the CPS. In particular, it did not all originate very close to the neutral sheet or at the

plasma sheet boundary layer. Wave-particle scattering is needed to divert perpendicular current and to increase the parallel current per unit flux tube at a given location. Electron scattering therefore appears to be distributed throughout the central plasma sheet.

[60] **Acknowledgments.** This material is based upon work supported by the National Science Foundation under grants ATM-9730845 and ATM-0122618 and by the NASA under grant NAG5-11820 at the University of New Hampshire. Research at the University of Iowa was supported by the NASA under grant NAG5-11485. The authors would like to thank S. Kokubun, who supplied full Geotail magnetic field measurements throughout the period studied.

[61] Lou-Chuang Lee thanks the two reviewers for their assistance in evaluating this paper.

References

- Angelopoulos, V., et al. (1993), Characteristics of ion flow in the quiet state of the inner plasma sheet, *Geophys. Res. Lett.*, *20*, 1711–1714.
 Baumjohann, W., G. Paschmann, and C. A. Cattell (1989), Average plasma properties in the central plasma sheet, *J. Geophys. Res.*, *94*, 6597–6606.
 Borovsky, J. E., R. C. Elphic, H. O. Funsten, and M. F. Thomsen (1997), The Earth's plasma sheet as a laboratory for flow turbulence in high- β MHD, *J. Plasma Phys.*, *57*, 1–34.

- Borovsky, J. E., M. F. Thomsen, and R. C. Elphic (1998), The driving of the plasma sheet by the solar wind, *J. Geophys. Res.*, *103*, 17,617–17,639.
- Büchner, J., and L. M. Zelenyi (1989), Regular and chaotic charged particle motion in magnetotail-like field reversals: I. Basic theory of trapped motion, *J. Geophys. Res.*, *94*, 11,821–11,842.
- Chen, J., and P. J. Palmadesso (1986), Chaos and nonlinear dynamics of single-particle orbits in a magnetotail-like magnetic field, *J. Geophys. Res.*, *91*, 1499–1508.
- Chew, G. F., M. L. Goldberger, and F. E. Low (1956), The Boltzmann equation and the one-fluid hydromagnetic equations in the absence of particle collisions, *Proc. R. Soc. London, Ser. A*, *236*, 112–118.
- Delcourt, D. C., and R. F. Martin Jr. (1999), Pitch angle scattering near energy resonances in the geomagnetic tail, *J. Geophys. Res.*, *104*, 383–394.
- Ferrière, K. M., and N. André (2002), A mixed magnetohydrodynamic-kinetic theory of low-frequency waves and instabilities in homogeneous, gyrotopical plasmas, *J. Geophys. Res.*, *107*(A11), 1349, doi:10.1029/2002JA009273.
- Frank, L. A., K. L. Ackerson, W. R. Paterson, J. A. Lee, M. R. English, and G. L. Pickett (1994), The comprehensive plasma instrumentation (CPI) for the GEOTAIL spacecraft, *J. Geomagn. Geoelectr.*, *46*, 23–37.
- Fritz, T. A., M. Alothman, J. Bhattacharjya, D. L. Matthews, and J. Chen (2003), Butterfly pitch-angle distributions observed by ISEE-1, *Planet. Space Sci.*, *51*, 205–219.
- Guéret, B., B. Lembège, and G. Belmont (1998), Laws for electron pressure variations across a collisionless shock, *J. Geophys. Res.*, *103*, 327–334.
- Hau, L.-N. (1996), Nonideal MHD effects in the magnetosheath, *J. Geophys. Res.*, *101*, 2655–2660.
- Heinemann, M., and R. A. Wolf (2001), Relationships of models of the inner magnetosphere to the Rice Convection Model, *J. Geophys. Res.*, *106*, 15,545–15,554.
- Hori, T., K. Maezawa, Y. Saito, and T. Mukai (2000), Average profile of ion flow and convection electric field in near-Earth plasma sheet, *Geophys. Res. Lett.*, *27*, 1623–1626.
- Huang, C. Y., and L. A. Frank (1994), A statistical survey of the central plasma sheet, *J. Geophys. Res.*, *99*, 83–95.
- Ichimaru, S. (1973), *Basic Principles of Plasma Physics: A Statistical Approach*, Benjamin, White Plains, N. Y.
- Iijima, T., and T. A. Potemra (1978), Large-scale characteristics of field-aligned currents associated with substorms, *J. Geophys. Res.*, *83*, 599–615.
- Israelevich, P. L., A. I. Ershkovich, and N. A. Tsyganenko (2001), Magnetic field and electric current density distribution in the geomagnetic tail, based on Geotail data, *J. Geophys. Res.*, *106*, 25,919–25,927.
- Ji, S., and R. A. Wolf (2003), Double-adiabatic MHD theory for motion of a thin magnetic filament and possible implications for bursty bulk flows, *J. Geophys. Res.*, *108*(A5), 1191, doi:10.1029/2002JA009655.
- Kan, J. R., and W. Baumjohann (1990), Isotropized magnetic-moment equation of state for the central plasma sheet, *Geophys. Res. Lett.*, *17*, 271–274.
- Kaufmann, R. L., and P. M. Kintner (1984), Upgoing ion beams: 2. Fluid analysis and magnetosphere-ionosphere coupling, *J. Geophys. Res.*, *89*, 2195–2210.
- Kaufmann, R. L., and C. Lu (1993), Cross-tail current: Resonant orbits, *J. Geophys. Res.*, *98*, 15,447–15,465.
- Kaufmann, R. L., C. Lu, and D. J. Larson (1994), Cross-tail current, field-aligned current, and B_z , *J. Geophys. Res.*, *99*, 11,277–11,295.
- Kaufmann, R. L., D. J. Larson, I. D. Kontodinas, and B. M. Ball (1997a), Force balance and substorm effects in the magnetotail, *J. Geophys. Res.*, *102*, 22,141–22,154.
- Kaufmann, R. L., I. D. Kontodinas, B. M. Ball, and D. J. Larson (1997b), Nonguiding center motion and substorm effects in the magnetotail, *J. Geophys. Res.*, *102*, 22,155–22,168.
- Kaufmann, R. L., B. M. Ball, W. R. Paterson, and L. A. Frank (2001), Plasma sheet thickness and electric currents, *J. Geophys. Res.*, *106*, 6179–6193.
- Kaufmann, R. L., C. Lu, W. R. Paterson, and L. A. Frank (2002), Three-dimensional analyses of electric currents and pressure anisotropies in the plasma sheet, *J. Geophys. Res.*, *107*(A7), 1103, doi:10.1029/2001JA000288.
- Kaufmann, R. L., W. R. Paterson, and L. A. Frank (2003), Birkeland currents in the plasma sheet, *J. Geophys. Res.*, *108*(A7), 1299, doi:10.1029/2002JA009665.
- Kistler, L. M., E. Möbius, W. Baumjohann, G. Paschmann, and D. C. Hamilton (1992), Pressure changes in the plasma sheet during substorm injections, *J. Geophys. Res.*, *97*, 2973–2983.
- Kokubun, S., T. Yamamoto, M. H. Acuna, K. Hayashi, K. Shiokawa, and H. Kawano (1994), The Geotail magnetic field experiment, *J. Geomagn. Geoelectr.*, *46*, 7–21.
- Larson, D. J., and R. L. Kaufmann (1996), Structure of the magnetotail current sheet, *J. Geophys. Res.*, *101*, 21,447–21,461.
- Northrop, T. G. (1963), *The Adiabatic Motion of Charged Particles*, Wiley-Interscience, Hoboken, N. J.
- Parker, E. N. (1957), Newtonian development of the dynamical properties of ionized gases of low density, *Phys. Rev.*, *107*, 924–933.
- Paterson, W. R., L. A. Frank, S. Kokubun, and T. Yamamoto (1998), Geotail survey of ion flow in the plasma sheet: Observations between 10 and 50 R_E , *J. Geophys. Res.*, *103*, 11,811–11,825.
- Rossi, B., and S. Olbert (1970), *Introduction to the Physics of Space*, McGraw-Hill, New York.
- Samsonov, A. A., and M. I. Pudovkin (2000), Application of the bounded anisotropy model for the dayside magnetosheath, *J. Geophys. Res.*, *105*, 12,859–12,867.
- Speiser, T. W. (1965), Particle trajectories in model current sheets: I. Analytic solutions, *J. Geophys. Res.*, *70*, 4219–4226.
- Stiles, G. S., E. W. Hones Jr., S. J. Bame, and J. R. Asbridge (1978), Plasma sheet pressure anisotropies, *J. Geophys. Res.*, *83*, 3166–3172.
- Tsyganenko, N. A., and D. P. Stern (1996), Modeling the global magnetic field of the large-scale Birkeland current systems, *J. Geophys. Res.*, *101*, 27,187–27,198.
- Tsyganenko, N. A., D. P. Stern, and Z. Kaymaz (1993), Birkeland currents in the plasma sheet, *J. Geophys. Res.*, *98*, 19,455–19,464.
- Usadi, A., R. A. Wolf, M. Heinemann, and W. Horton (1996), Does chaos alter the ensemble averaged drift equations?, *J. Geophys. Res.*, *101*, 15,491–15,514.
- Vasyliunas, V. M. (1970), Mathematical models of magnetospheric convection and its coupling to the ionosphere, in *Particles and Fields in the Magnetosphere*, edited by B. M. McCormac, pp. 60–71, D. Reidel, Norwell, Mass.
- Weimer, D. R. (2001), Maps of ionospheric field-aligned currents as a function of the interplanetary magnetic field derived from Dynamics Explorer 2 data, *J. Geophys. Res.*, *106*, 12,889–12,902.
- Wolf, R. A. (1983), The quasi-static (slow-flow) region of the magnetosphere, in *Solar-Terrestrial Physics: Principles and Theoretical Foundations*, edited by R. L. Carovillano and J. M. Forbes, pp. 303–368, D. Reidel, Norwell, Mass.
- Zmuda, A. J., and J. C. Armstrong (1974), The diurnal flow pattern of field-aligned currents, *J. Geophys. Res.*, *79*, 4611–4619.

L. A. Frank and W. R. Paterson, Department of Physics and Astronomy, University of Iowa, Iowa City, IA 52242-1479, USA. (frank@iowasp.physics.uiowa.edu; paterson@iowasp.uiowa.edu)

R. L. Kaufmann, Department of Physics, University of New Hampshire, DeMeritt Hall, 9 Library Way, Durham, NH 03824-3568, USA. (dick.kaufmann@unh.edu)